Combining coronagraphy with interferometry as a tool for measuring stellar diameters

P. Riaud[1], C. Hanot[1]

Université de Liège, 17 Allée du 6 Août, B-4000 Sart Tilman, Belgium

riaud.pierre@gmail.com

hanot@astro.ulg.ac.be

ABSTRACT

The classical approach for determining stellar angular diameters is to use interferometry and to measure the fringe visibilities. Indeed, in the case of a source having a diameter larger than typically $\lambda/6B$, B being the the interferometric baseline and λ the wavelength of observation, the fringe contrast decreases. Similarly, it is possible to perform angular diameter determination by measuring the stellar leakage after a coronagraphic device or a nulling interferometer. However, all coronagraphic devices (including those using nulling interferometry) are very sensitive to pointing errors and to the size of the source, two factors with a significant impact on the rejection efficiency. In this work we present an innovative idea for measuring stellar diameter variations, combining coronagraphy together with interferometry. We demonstrate that, using coronagraphic nulling statistics, it is possible to measure such variations of angular diameters down to $\approx \lambda/40B$ with 1σ error-bars as low as $\approx \lambda/1500B$. For that purpose, we use a coronagraphic implementation on a two-aperture interferometer, a configuration that increases significantly the precision of stellar diameter measurements. Such a design offers large possibilities regarding the stellar diameter measurement of Cepheids or Mira stars, at a 60-80 μas level. We report on a simulation of a measurement applied to a typical Cepheid case, using the VLTI-UT interferometer at Paranal.

Subject headings: instrumentation: high angular resolution, instrumentation: interferometers, methods: statistical, techniques: photometric

1. Introduction

Cepheid variable stars consist of unique standard candle for the determination of extra-galactic distance scales (Vilardell et al. 2007; Feast et al. 2008). However, even for the nearby Cepheids, precise distance measurements are extremely challenging due to their small stellar angular diameters ($< 3mas$). Thanks to the use of optical interferometry, it has been possible, since a decade, to directly measure the angular diameter variations of δ Cep, and to combine them with radial velocity measurements to derive its distance (Mourard et al. 1997). Unfortunately, due to its actual limitation in terms of angular resolution, classical interferometry (i.e. that of visibility measurements) is not sensitive enough to measure the pulsation of more distant Cepheids (Mourard et al. 1994; Armstrong et al. 2001; Kervella et al. 2001). Indeed, with classical stellar interferometry, a stellar angular diameter is measured by fitting the corresponding visibility profile with a Bessel $J1$ function. Under good observing conditions, this technique allows typical precision on stellar diameters determination of $500 \pm 200 \mu as$ at $1.65 \mu m$ on the VLT-UT largest baseline (UT1-UT4 130m). Even though such precision is enough in the case of closeby Cepheids, this approach fails to detect fine stellar atmosphere pulsations of more distant Cepheids or Mira stars (> 1 Kpc), which have typical angular diameters of $60 - 80 \mu as$ with variations of $\sim 2 \mu as$. As a consequence, the number of available extragalactic distant-scale calibrators is significantly reduced. Obtaining higher accu-

racy measurements could help setting better constraints on the previous period-radius and period-mass relations, with a direct impact on the extragalactic distance scale studies (Macri et al. 2006; Ferrarese et al. 2007; van Leeuwen et al. 2007; Vilardell et al. 2007; Feast et al. 2008).

In this paper we suggest the use of an innovative configuration, based on the implementation of the coronagraphy principle to a multi-aperture interferometer. Combination of these two techniques (interferometry and coronagraphy, or equivalently, nulling interferometry) is generally used to improve the detection of faint structures or companions around nearby stars (Riaud et al. 2002; Tinetti 2006; Wallner et al. 2006). Given the fact that coronagraphic devices are sensitive to the angular source size, a coronagraphic implementation of a stellar interferometer can further improve the detection of stellar sources diameter variations.

In order to derive distance estimates when using an interferometer in the visibility mode, the Cepheid diameter measurements can be combined with the radii derived from the stellar flux and radial velocity curves. Our technique, based on statistics on the best nulling rejection of the coronanagraphic device, measures directly the stellar diameter. The nulling varies with the square of the stellar diameter, with a large variation in the first Airy ring of the coronagraphic image. Indeed, a change of the source diameter has an impact on the intensity of the residual speckles included in the first Airy ring, which is proportionnal to the square of the angular diameter (see Eq. 2). We use the null depth leakage on a ground-based interferometer, operating in speckle mode (i.e. using short exposure times), to measure the stellar diameter with a sub-resolution precision ($\approx \lambda/40B$ with $\pm 1\sigma$ error-bars as low as $\approx \lambda/1500B$, where λ is the wavelength of observation and B the interferometer baseline). Compared to the classical visibility measurement where $V^2 \approx 1$ for a sub-resolution stellar diameter, a coronagraphic device allows to reject the coherent part of the interferometric pattern and enhances fine photometric variation due to the angular diameter. The gain is directly proportionnal to the rejection factor of the coronagraphic mask. The proposed technique can be applied to extended envelopes around Cepheids (Mérand et al. 2007) or Mira stars. Compared to continuum observations, it

makes possible to highlight the fine diameter variations of extended envelopes in $H\alpha$ (in the visible) or $Br\gamma$ (in the near infrared), with the simultaneous use of two channels (differential imaging).

2. Nulling interferometry principle

2.1. Coronagraphic nulling function

Considering an image obtained in coronagraphic mode with a vortex coronagraph (Mawet et al. 2005) on a uniform circular aperture, the coronagraphic attenuation f_{ca} can be approximated by:

$$f_{ca}(x) \approx 1 - \frac{4J_1^2(\pi x/\sqrt{3})}{(\pi x/\sqrt{3})^2} \tag{1}$$

where $f_{\mathrm{ca}}(x)$ is the function of the coronagraphic attenuation relative to the angular distance (x) measured in λ/d, d beeing the aperture diameter. These results (Mawet et al. 2005) take into account the full Inner Working Angle of the coronagraphic mask. Under such conditions, a limited development of the above expression near the center, $f_{\mathrm{ca}}(x)_{LD}$, is given by:

$$f_{ca}(x)_{DL} \approx (\pi^2 x^2/6) \tag{2}$$

Defining the nulling ratio as $R_\alpha = 1/f_{\mathrm{ca}}$, we conclude that, near the center of a coronagraphic image R_α, is inversely proportional to x^2, the square of the angular size of the source . For the case of a resolved source and a circular pupil coronagraph (Riaud et al. 2002), the total rejection factor is given by:

$$R_\alpha = \frac{\int_0^\alpha x \cdot dx}{\int_0^\alpha f_{ac}(x) \cdot x \cdot dx} \tag{3}$$

$$R_\alpha \approx \frac{\alpha^2}{2} \left[\int_0^\alpha f_{ac}(x)_{DL} \cdot x \cdot dx \right]^{-1} = \frac{12}{\pi^2 \alpha^2} \tag{4}$$

In the above calculations we considered a "top hat" stellar diameter (2α) with no limb darkening. In the case of a two apertures interferometer, the integration variable x is in units of λ/B. The effect of nulling on stellar diameter measurements is more important in the center of the coronagraphic image, and in nulling interferometry projects such as DARWIN or TPF (Wallner et al. 2006) it is generally referred to as "stellar leakage". This effect has been extensively studied in the nulling mode

for TPF-I/DARWIN and coronagraphic mode for TPF-C programs.

However, the effect of the atmospheric turbulence imposes strong limitations on the nulling performance of a coronagraph (Riaud et al. 2003; Jenkins 2008). To evaluate these limitations, all interferometric simulations used in this paper have been carried out under realistic atmospheric turbulence conditions. In the next section, we explain the possible coronagraphic configuration that could be used in the VLTI interferometer (UT1-UT4) to perform the best possible stellar diameter retrieval.

2.2. Interferometric recombination with a coronagraph

The principle of the instrument we describe in this paper is somewhat different from usual coronagraphs where the masks are used in the focal plane of a single mirror. Instead, we propose to recombine two or more beams directly on a phase mask coronagraph (Fizeau Mode). First, the light coming from the telescopes is injected into monomode fiber bundles, therefore filtering the input pupils (see Fig.1). The main advantages of this technique are first that it allows to simplify the interferometric recombination (Riaud et al. 2001b) and second that it apodizes the entrance pupil of the Fizeau recombination which partially removes the effect of the central obscuration of the telescopes. These two advantages help the system (and therefore the rejection factor) to be more robust to the external fluctuations (strehl, tip-tilt, ...). The main drawback however is that these injections into monomode fibers decrease the overall throughput of the instrument by about 25%, depending on the design and on the residual tip-tilt. At the output of the fiber bundles, the two interferometer's arms are focused onto a phase mask coronagraph such as the Four Quadrant Phase-Mask (FQPM, Rouan et al. 2000; Riaud et al. 2001a) or the Annular Grove Phase-Mask (AGPM, Mawet et al. 2005) or Vortex phase-mask (Swartzlander et al. 2008) (see Fig. 1). Inserting such masks at the focal plane of the interferometer allows direct nulling of a source located on the optical axis of the system with no additional steps. The problem, however, is that the resulting coronagraphic image is too diluted (in several thousands of speckles) to be usable. A densification stage must therefore be added after the Lyot stops to increase the signal to noise ratio (see Sect. 3.2). After the coronagraph, the two beams are collimated so that the Lyot stops can be used (just like in usual coronagraphy designs), the only difference being that we have two coronagraphic pupils instead of one. At this stage, a near-infrared photodiode with overall quantum efficiency of 25% (Wu et al. 2009; Myers et al. 2006; Hicks et al. 2003) can be placed in front of the entire pupil in order to monitor the photometric variations of the interferometer. This important information can be later used to significantly increase the precision on the measurement by applying some corrections to the measured rejection factor. Finally, the last step before the final interferometric recombination is the densification of the two beams (Labeyrie 1996). As already explained, this important step increases dramatically the signal-to-noise ratio in a narrow field of view (Riaud et al. 2001b), allowing us to perform coronagraphic measurements with very short integration times which is mandatory in order to get non-zero probabilities of measuring high rejection ratios. The densification is a very simple two-step process :

(a) First, both beams are expanded using two diverging lenses (one for each channel), while the separation between them is kept constant.

(b) Then, once there is almost no gap left between them, another set of two converging lenses are used to perform the collimation[1]. In the final image plane (D2, see Fig.1), a densified coronagraphic image is generated in the first lobe of the Airy pattern (corresponding to a field of view of three fringes).

One of the main advantages of this instrument compared to usual long baseline interferometers is that all the optics that come after the pupil injection into the single-mode fibers are fixed. The resulting workbench is therefore much more simple and stable. Despite this fixed optical scheme, one must not forget that the real projected baseline on the sky changes during observation, and so does the rejection factor. This effect must be taken into account during the coronagraphic data analysis.

---

[1]On a technical point of view, these lenses (or micro-lenses) could be manufactured in infrasil so that they would be usable from I to K band.
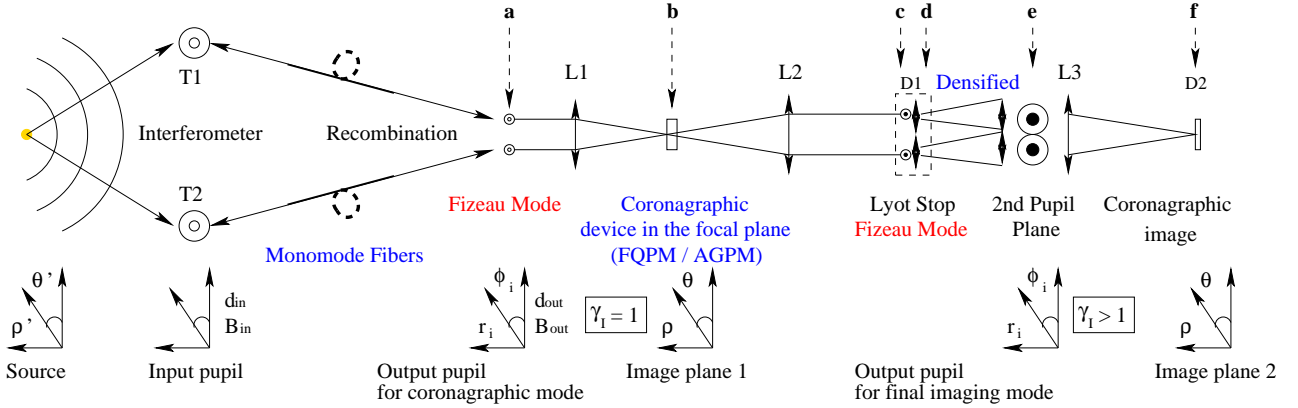
Fig. 1.— Optical scheme of the proposed implementation of coronagraphy on an interferometer with two apertures. On the left part of the graph, the interferometer (T1, T2) is combined with monomode fiber bundles on a Fizeau mode imaging. The L1 lens forms the interferometric Fizeau image on the FQPM/AGPM coronagraph (first focal plane). The L2 lens images the pupil in the second plane, while the Lyot stop suppresses the diffracted starlight. The photodiodes D1 (in the pupil plane) are monitoring the rejection factor (see Fig. 3). After the Lyot stop, the apertures are recombined using a densified pupil, to increase the signal-to-noise ratio in the central fringe. Finally, L3 forms the coronagraphic images (second focal plane) on the high speed detector D2 in the interferometric field of view (see Fig. 2). More details about the optical and numerical implementation of steps a-f can be found in Fig. 2. We also present all coordinate systems used in Sect. 3. Concerning the two pupil planes and the two focal planes, we use the same coordinates (r_i, ϕ_i), and (ρ, θ) respectively needed in the mathematical considerations. Thus, the Fizeau and the densified modes are explained within the same theory.

The main nulling efficiency limitation for all coronagraphic ground-based devices is the atmospheric turbulence. Indeed, the tip-tilt noise has a major weight as it influences the centering of the central fringe on the coronagraphic device. As explained above, in order to have a significant amount of coronagraphic measurement with high contrast ratios, it is mandatory to have high frequency detectors (up to 100 Hz for K band and 1 kHz for I band) in order to follow the lifetime of the speckles (Labeyrie 1970) and prevent any averaging of the nulling measurements. Within a dataset, the majority of the frames give an image which is not centered on the coronagraph because of the poor Strehl ratios. They are characterized by weak attenuation factors, while the few ones with a good centering have higher attenuation factors. Therefore, by taking several thousands of short-exposure coronagraphic images ($> 10^4$), it is possible to obtain frames with nulling greater than $20 - 100$ in their center (see Section. 6.1), which is a requirement to emphasize the contribution of the stellar diameter variations.

Another limitation is the photometric fluctuations. To prevent this effect, the total flux can be monitored in both the coronagraphic pupil and the image plane during the acquisition process. The relative photometry between the rejected starlight in the pupil plane and the residual image is mandatory in order to properly calibrate the nulling ratio of the interferometric system, but an absolute photometry is not necessary for this case. The photometry requirement is similar to the interferometric visibility measurement, for which 1 to 3 % is needed. As the Cepheids undergo intrinsic luminosity variations, an effect that is detectable with a full data analysis, it is possible to study the correlation between the diameter retrieved by our method and the absolute luminosity variations. The detailed design of the coronagraphic implementation on the two-aperture interferometer proposed in the current work is presented in Fig. 1.

3. Mathematical considerations

3.1. Interferometric configurations

This section provides the mathematical background needed to understand the coronagraphic effect on an interferometer. The numerical simulations presented in subsequent sections are based on the latter principle. Indeed, we propose in the first stage (before the coronagraph) to use direct Fizeau interferometric imaging followed by the densified interferometric mode after the Lyot stop (the second stage). The difference between these two modes is simply given by the densification factor γ_I and all the mathematical developments are common for both densified and non-densified recombinations.

The first recombination method used is the one introduced by H.Fizeau (1868) and consists in making direct homodyne combination of the sub-apertures without changing the relative sub-pupil sizes of the system. The pupil transform is strictly homothetic between the input and the output interferometric pupil with $\gamma_I = 1$ (see Eq. 7). The densified recombination case is characterized by $\gamma_I > 1$. We will explain the general case, where the homothetic pupil transformation between the input and the output pupil changes the optical path by a factor γ_I. The case of full densification of only two telescopes is called Michelson recombination (Michelson 1891; Michelson & Pease 1921). For that, we must consider three different planes to calculate the image properties for various interferometers: (a) the input pupil plane (telescopes), (b) the output pupil plane in the optical system and (c) the plane where the final image is generated (see Fig. 1). In the case of a global pupil transform we can define the ratio coefficient after the pupil remapping as:

$$\gamma_d = d_{out}/d_{in} \qquad (5)$$
$$\gamma_b = B_{out}/B_{in} \qquad (6)$$
$$\gamma_I = \gamma_d/\gamma_b \qquad (7)$$

where d_{out}, d_{in} are the the respective diameters of the sub-aperture in the output and input pupil plane, and B_{out}, B_{in} are the baselines of the interferometric array in the two latter planes. The dilution factor of the interferometric scheme becomes B_{out}/d_{out} after the pupil remapping.

The position of the telescopes in the pupil plane of the interferometer can be described by means of Dirac positions (δ) for the ith aperture in the $r_i.e^{i\phi_i}$ polar coordinate system (see Fig. 1). It should be noted that even though the coronagraphic mode is that of Fizeau, the final image is in the densified mode. We use the same notation for the new position of the telescopes after the densified process in the pupil plane to describe the properties of the interferometric images ((r_i, ϕ_i), see Fig. 1). The coordinates (ρ', θ') and (ρ, θ) are the position vectors in the source and image plane, respectively.

It is possible to calculate the optical transfert function (OTF) for a general interferometric scheme in the following way:

$$OTF(\rho, \theta, \rho', \theta') = \left| T_{(a, \gamma_d)} \cdot I_{(\delta, \gamma_b)} \right|^2 \qquad (8)$$

where $T_{(a, \gamma_d)}$ is the envelope function given by the diffraction pattern of a sub-aperture and $I_{(\delta, \gamma_b)}$ is the interferometric pattern given by the position δ of the telescopes in the frequency domain.

The envelope pattern in the case of a circular aperture with central obscuration a with $a < 1$ is a pure radial function. It can be easily calculated in the following way:

$$
\begin{aligned}
T_{(a, \gamma_d)} &= \frac{2J_1(\pi \cdot d_{out}(\rho - \rho'/\gamma_d)/\lambda)}{\pi \cdot d_{out}(\rho - \rho'/\gamma_d)/\lambda} \\
&- \frac{2J_1(\pi \cdot a \cdot d_{out}(\rho - \rho'/\gamma_d)/\lambda)}{\pi \cdot a \cdot d_{out}(\rho - \rho'/\gamma_d)/\lambda}
\end{aligned}
\qquad (9)
$$

Where $\rho - \rho'/\gamma_d$ denotes the homothetic pupil transformation effect on the source position in the final image plane. For an off-axis source (radial position ρ' relative to the center), the envelope is shifted to a lower angular position ρ'/γ_d. Note that this envelope solution is generalizable for various shapes of pupil.

In the same manner, we calculate the interferometric pattern function given by the Fourier transform of the Dirac pattern telescope position in the frequency domain:

$$CS_{\theta, \phi_i} = cos(\theta) \cdot cos(\phi_i) + sin(\theta) \cdot sin(\phi_i) \qquad (10)$$
$$CS_{\theta', \phi_i} = cos(\theta') \cdot cos(\phi_i) + sin(\theta') \cdot sin(\phi_i) \qquad (11)$$
$$I_{(\delta, \gamma_b)} = \sum_i^n exp - \frac{2i\pi \cdot r_i}{\lambda} \left(\rho\, CS_{\theta, \phi_i} - \frac{\rho'}{\gamma_b} CS_{\theta', \phi_i} \right) \qquad (12)$$

where n is the number of sub-apertures and $\rho, \rho'/\gamma_d$ denote the same homothetic pupil trans-

formation effect on the source position on the final image plane. If we denote as $O(\rho', \theta')$ the object intensity distribution, we can derive the intensity distribution (Eq. 8):

$$I_{obj}(\rho, \theta) = \int_\lambda \int_{\rho'} \int_{\theta'} O(\rho', \theta') \cdot OTF(\rho, \theta, \rho', \theta') \cdot d\rho' \cdot d\theta' \cdot d\lambda \tag{13}$$

- The Fizeau case corresponds to $\gamma_I = 1$ where the convolution relationship is kept during this recombination. For off-axis sources, the displacement of the interferometic pattern given by the multiple sub-apertures $I_{(\delta, \gamma_b)}$ follows perfectly the displacement of the telescope diffraction pattern $T_{(a, \gamma_d)}$.
  The result is a real PSF where the fringe pattern is modulated by a large diffraction disk. For a large dilution factor (small diameter of sub-apertures and long baselines), the focal plane image features one white fringe and many (hundred or more) dispersed fringes. Only a fraction of the energy is in the white fringe.

- In the densified mode, where $\gamma_I > 1$, there is no simple convolution relationship anymore between the object and the transfer function of the interferometer. Indeed, the interferometric pattern $I_{(\delta, \gamma_b)}$ moves faster by a factor γ_I than the new telescope diffraction pattern after the pupil remapping.
  The final image of the observed object is in a narrow field of view delimited by the new telescope diffraction envelope $T_{(a, \gamma_d)}$. The main properties of the densified image is that the astrophysical object observed by the first mirrorx of the telescope (λ/d_{in}) is compressed in this new narrow field of view (λ/d_{out} called "Zero Order Field" in Labeyrie (1996); Riaud et al. (2001b); Riaud (2003)) with a limited number of resolution elements.

3.2. Coronagraphic configurations

In this section, we present the rejection effect of a phase-mask coronagraph on the Fizeau interferometric configuration. The coronagraph is working in coupled mode on all apertures (i.e. on the Fizeau PSF) rather than independently on

each telescope. Under this condition, the coronagraphic pupil acts on the full amplitude image function and shows a cross talk effect by mutual contamination of the rejected starlight in each sub-aperture. In the first order, the following calculus shows that the cross talk effect is of minor importance, and that the coronagraphic rejection is mainly driven by the differential piston on each telescope of the interferometric system. We shall now demonstrate these properties by applying the vortex phase-mask on the Fizeau image.

Let us present the coronagraphic phase-mask function, M_c, in the ideal case of vortex coronagraph of order 2 (Mawet et al. 2005):

$$M_c = e^{\pm i2\theta} \tag{14}$$

where θ is the angular coordinate in the coronagraphic focal plane.

With Fizeau recombination, the amplitude image is given directly by the sub-aperture pattern $T_{(a, \gamma_d)}$ modulated by the interferometric fringes $I_{(\delta, \gamma_b)}$. The amplitude of the coronagraphic image, A_{CI}, after the coronagraphic phase-mask effect can be expressed directly in the Fizeau case by:

$$A_{CI} = T_{(a, \gamma_d)} \cdot I_{(\delta, \gamma_b)} \cdot M_c \tag{15}$$

Mawet et al. (2005) has demonstrated that, in the pupil plane, the diffracted starlight by a vortex coronagraph has the following form:

$$\Pi_c(r, \theta) = \epsilon_{\lambda, i} \qquad r < d_{out}/2 \tag{16}$$

$$\Pi_c(r, \theta) = \frac{e^{\pm i2\phi}}{(2r/d_{out})^2} \qquad r > d_{out}/2 \tag{17}$$

where $\epsilon_{\lambda, i}$ is the coronagraphic residual in the ith sub-pupil due to wavefront errors, the telescope central obscuration and the mask chromatism limitation. Under this condition, at the exit pupil plane of the Fizeau interferometer after a vortex coronagraph, the diffracted light possesses two differents terms:

$$\Pi_{Fc}(r, \theta) = \sum_i^n (\epsilon_{\lambda, i} + E_{c, i}) \tag{18}$$

where $E_{c, i}$ is the cross-talk energy between the different pupils. The cross-talk energy between pupils i and j is given by:

6

$$E_{c,i} = \frac{d_{out}^2}{4} \cdot \left| \sum_{j \neq i}^{n} \int_0^{\frac{d_{out}}{2}} \int_0^{\alpha_m} \frac{e^{\pm i2\phi} \cdot r \cdot dr \cdot d\phi}{(r - (r_j - r_i))^2} \right|_i^2$$

(19)

with

$$\alpha_m = 2 \cdot \arctan(d_{out}/(r_j - r_i)))$$

(20)

In the case of the Fizeau recombination of the two VLT-UT1/UT4 telescopes we may calculate the cross-talk term with r_j-r_i=B_{out}/d_{out}=16.25, $\gamma_I = 1$ and finally, by considering $E_{c,1} \approx E_{c,2}$. As a consequence, from Eq. 19 we derive: $E_{c,i} = 9.35.10^{-7} << \epsilon_{\lambda,i}$.

Phase-mask coronagraphs such as the FQPM or the OVVC have been tested on optical testbenches from visible (Riaud et al. 2003) to near-infrared (Mawet et al. 2009) wavelengths and the obtained attenuation factors obtained are greater than 1000 in full band-pass (R=5) and $> 10^5$ in narrow band-pass (R=300). Under such conditions, some manufacturing defects or limitations appears to be negligible in our configuration. Indeed, the main limitation of the coronagraphic rejection in the Fizeau configuration ($\epsilon_{\lambda,i}$) is due to the residual atmospheric piston between the two apertures.

3.3. Differential piston

In this section, we describe the effect of differential piston on an interferometer. A long baseline interferometer tends to amplify the wavefront tip and tilt in the different sub-apertures introduced by the atmospheric turbulence ($\lambda/d \rightarrow \lambda/B$). Equation 12 gives the differential piston term for different recombination schemes. Concerning the Fizeau configuration ($\gamma_I = 1$), the differential piston effect can be easily seen as the full PSF pattern moving in front of the coronagraphic device. The coronagraph is highly sensitive to tip-tilt errors and the rejection factor takes a dive. Under such a condition, it is mandatory to follow the image with a fringe tracker ($< \lambda/2$ rms) in order to keep the rejection high enough. In this paper, we consider a rather pessimistic case with a fringe tracker having an error of $\lambda/3$ rms in the H-band (500 nm rms). The Finito and Prima instruments on the VLTI for example provide a smaller differential piston error (Le Bouquin et al. 2008, 2009; van Belle 2009).

The final configuration after a proper coronagraphic pupil filtering is densified to increase signal to noise ratio. This second stage of densification artificially creates wavefront stairs in each sub-pupil with an important tip-tilt, and it can be seen as a high fringe moving in the limited field of view given by the densification process. If the fringe tracker residual remains below $< \lambda/2$ rms the densified image is of zero order (white fringes) in the limited field of view of the "Zero Order Field". In terms of the Fourier frequencies, all high order images (dispersed peaks) present in the Fizeau mode are folded in the zero order to increase the signal.

3.4. The monomode fiber telescope link

For our Fizeau recombination in the near infrared, we preferred to use single-mode optical fibers (Shaklan 1990; Coudé Du Foresto 1997; Wallner et al. 2002) rather than bulk optics, as they provide a more flexible and compact solution for a beam combination. The spatial filtering properties of single-mode fibers are used to properly convert random atmospheric phase perturbations into photometric fluctuations. Phase-mask coronagraphy seems to be more robust to photometric fluctuations in the pupil plane than to phase ones (Riaud et al. 2001a). Nevertheless, although in this case the atmospheric jitter decreases, high frequency noise starts to be present in the amplitude measurements. The configuration allows better nulling rejection on the center but increases speckle noise (amplitude fluctuation) at high frequencies.

The fundamental mode field distribution for a single-mode fiber corresponds to the Bessel functions J_1 near the center ($r < 0.5\,\omega_0$) and a K_1 Bessel for $r > 0.5\,\omega_0$, where ω_0 is the radius of the fiber waist (see Eq. 23). We can however approximate with very good accuracy ($\approx 2\%$) the fundamental mode field distribution in each sub-aperture pupil (Π_{Ai}) using a Gaussian function:

$$\Pi_{Ai} = A_i \cdot \frac{\omega_0}{\omega_z} . e^{-r_i^2/\omega_z^2}$$

(21)

$$\omega_z = \omega_0 \cdot \sqrt{1 + (\lambda z/\pi\omega_0^2)^2}$$

(22)

$$\omega_0 \approx a \cdot \left(0.65 + \frac{1.619}{V^{1.5}} + \frac{2.879}{V^6}\right) \quad (23)$$

$$V = 2\pi \cdot NA \cdot a/\lambda \quad (24)$$

$$NA = \sqrt{n_c^2 - n_g^2} \quad (25)$$

where ω_0 is the waist of the fiber corresponding to the minimum size of irradiance in the output fiber ($\approx 3 - 10\,\mu m$), a the radius of the fiber core ($\approx 3 - 6\,\mu m$), V is the normalised cutoff frequency (the fiber is monomode if $V < 2.405$), NA the numerical fiber aperture given by the index of refraction of the core material, n_c and n_g the refraction indices of the cladding material ($NA = 0.12 - 0.2$) and ω_z the mode field distribution irradiance at a distance z.

Due to an infinite extension of the Gaussian distributions, the mode field distribution must be truncated on each sub-pupil by a diaphragm $\Pi_D = d_{out}$. The envelope $T_{(a,\gamma_d)}$, previously described by a simple Bessel function in the case of the classical circular aperture $(2J_1(\rho)/\rho)$, must be replaced by a new one, obtained from the Hankel transform H of Π_{Ai} in order to include the diaphragm effect. In this case, Π_{Ai} (see Eq. 27) depends on the propagation distance z_{out} within the injection system:

$$d_\omega = \frac{d_{out}}{2\omega_0 \cdot \sqrt{1 + (\lambda z_{out}/\pi\omega_0^2)^2}} \quad (26)$$

$$\Pi_{Ai} = \frac{A_i \cdot e^{-d_\omega^2 r_i^2/d_{out}^2}}{\sqrt{1 + (\lambda z_{out}/\pi\omega_0^2)^2}} \quad (27)$$

$$T_{z_{out}} = H\left[\Pi_{Ai} \cdot \Pi_D\right] \quad (28)$$

$$T_{z_{out}} = \frac{2A_i \cdot e^{-d_\omega^2 \rho^2/d_{out}^2}}{\sqrt{1 + (\lambda z_{out}/\pi\omega_0^2)^2}} \frac{J_1(\pi \cdot d_{out}\rho/\lambda)}{\pi \cdot d_{out}\rho/\lambda} \quad (29)$$

The final envelope is a Gaussian function modulated by a Bessel J_1 function, due to the presence of the diaphragm in the pupil plane. Compared to the previous mathematical development, the envelope image does not possess the $\rho - \rho'/\gamma_d$ term as the classical diffraction envelope. The advantage of using monomode fibers is that they strongly attenuate the tip-tilt term in each sub-pupil and at the same time there remains only a piston term between all sub-pupils.

If only the center of the fundamental mode is used, the irradiance distribution is almost uniform in each sub-pupil, but the total injection efficiency ($< 15\%$) of the beams drops significantly. Now, if a large part of the Gaussian irradiance distribution in each pupil is used, the strong apodization function rejects the flux in the second lobe of the Bessel function and the total efficiency remains also low. Therefore, the optimal size of the diaphragm radius is around 0.8 to 1.2 $\omega_{z_{out}}$, with the total efficiency becoming $\approx 20 - 25\%$. This value corresponds to the matching between the fundamental mode of the fiber and the energy in the first λ/d of the perfect telescope PSF (see Section 4).

The polarization maintaining fibers (Delage & Reynaud 2001) seems to be less efficient regarding the nulling rejection of the coronagraph than the classical circular fibers due to a possible mode ellipticity. Indeed, the mode is elliptic and no matching of the azimuthal symmetry of all phase-mask coronagraphs can be used in this experiment. Finally, the dispersion correction of the long monomode fiber links can be done by including a small portion of photonic fused-silica fibers ($1 - 2$ meters) that create negative dispersion for an optimized central wavelength.

4. Numerical simulations

To study the effect of coronagraphic nulling on stellar diameters we have performed numerical simulations. To make our study as realistic as possible, we have considered a single-layer atmospheric turbulence (Von Karman statistics) to which a random tip-tilt (Gaussian statistic) and piston noise have been added to the pupil plane (Fig. 2a). We assume a residual tip-tilt of 8 mas rms between the two apertures, a Fried parameter of $r_0 = 15$ cm, and an outer scale of 25 m in the visible band (Paranal atmospheric characteristics). The adaptive optics is a low-order AO with a tip-tilt mirror (5 mas rms) on each VLT telescope (Bonaccini et al. 1997) and with a partial correction of the first order aberrations (Zernike polynomial 2 to 9 and Strehl ratio of $\approx 30\%$ in H-band). The fringe tracker is simulated as a low-pass filter having a frequency noise distribution following a $1/f$ law and a correction accuracy expressed in terms of a wavelength fraction. Finally, we have added to the simulations of the photometric measurements in full H-band: (i) photon and readout noises ($6\,e^-$), (ii) noise due to saturation
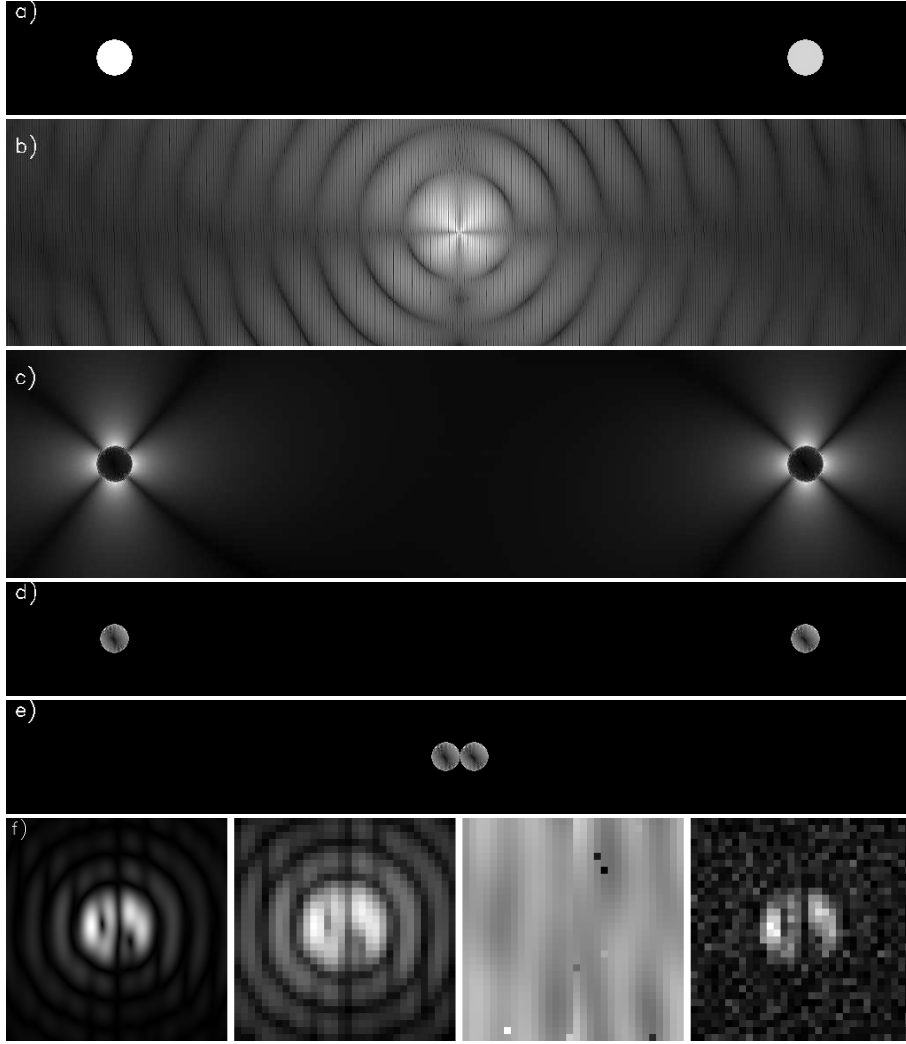
Fig. 2.— Numerical simulation illustrating the principle of coronagraphy with an interferometer, implemented on a UT 1−UT 4 VLTI configuration, using a 130 m baseline. *Panel a:* The two entrance interferometric pupils are shown in the case of low differential piston (1 mas rms here). To make the simulations more realistic, turbulence and tip-tilt noise before a proper monomode filtering have been included. *Panel b:* Direct Fizeau PSF image obtained on the AGPM coronagraphic mask. This image is seen in intensity for a circular entrance polarization. We notice a relatively bad centering of the stellar fringes with respect to the coronagraphic mask and the presence of a singularity in the mask center (vortex phase-mask). *Panel c:* Coronagraphic pupil plane, seen without the use of a diaphragm, *Panel d:* Coronagraphic pupil plane, seen after the use of a simple diaphragm. *Panel e:* Coronagraphic pupil plane, after the densification process, where the two pupils are joined. *Panel f:* Residual coronagraphic images in densified mode (left to right) *Panel f1:* Central part of a densified coronagraphic image calculated by the simulation. *Panel f2:* Same image as in panel f1, but with a proper detector sampling (32×32 pixels), after pixel averaging. *Panel f3:* Image of the residual flat ($\pm 1\%$ PTV) added on the coronagraphic image to mimic the data analysis limitation. *Panel f4:* The final image, which includes flat, readout (6e-) and photon noise, was considered (during the simulations) to be taken at a low signal-to-noise ratio ($max \approx 1800$ ADU, for a bias of 500 ADU). We notice the difference of the fringe scale in the Fizeau mode (panel b) and the final densified mode. The brightness scale in the images is non-linear.

9

effects ($10^5\,e^-$) and (iii) a residual flat noise ($\pm 1\%$ PTV).

The effect of stellar diameter variations on the nulling is calculated as follows: we create a coronagraphic image template using a total of 113 pixels that cover the requested stellar diameter with a uniform statistic. A limb-darkened law for the stellar luminosity decreases the effective diameter by about 5%. On every frame, any possible instrumental limitation, such as residual chromatism on the phase mask, are included in addition to the turbulence effect. We assume a uniform diameter for the observed star. In this way, this image is a signature of the coronagraphic response of the stellar radius with respect to the interferometric configuration.

Each short coronagraphic exposure is then calculated using a large sampling (2048×2048 pixels), to minimize the aliasing effect due to the interferometric configuration (considering an interferometric baseline of 780 pixels – 130 m –). Each final image is finally downsampled to 32×32 pixels to mimic the sampling of the detector corresponding to a field of view of $\approx 10\lambda/B$ on each side of the detector, with 3 pixels per λ/B. Indeed, in order to allow high speed frames recording, a smaller detector is needed. A NICMOS technology in the near infrared with a 32×32 pixels detector can allow a 500 Hz frame rate, which is sufficient for the J, H, and K bands. Finally, as in this interferometric mode the (narrow) central field of view contains all information for a proper visibility retrieval, we suggest to use the densified configuration, combined with a 32×32 pixels detector to increase the signal to noise ratio (Riaud et al. 2001b). In order to perform a "dark speckle" analysis (Labeyrie 1995), and follow the seeing variations, it is essential to obtain a large number of frames. As each frame corresponds to a single speckle realization ($\tau = 3$ ms in the visible, $\tau = 20$ ms in the K band, see Table 3), the probability to obtain a high starlight coherence in the data set (Strehl Ratio > 30%) is less than 10% (see Fig. 4). To increase the interferometric throughput in the monomode fiber, we only make use of low order adaptive optics for atmospheric piston and tip-tilt correction.

In order to obtain the best-value of coronagraphic nulling, the stabilization of the Optical Path Difference (OPD) between the two apertures can be achieved using a fringe tracker. The nulling factor in the center of the stellar peak is generally small, varying from ≈ 20 when no fringe tracker is used, to $40 - 150$ when a fringe stabilizer such as FINITO (Le Bouquin et al. 2009) or PRIMA (van Belle 2009) is used due to the significant seeing variations. Nevertheless, for a high strehl ratio (> 50%), the effect of the resolved source can be seen with the coronagraphic device. The numerical simulation requires $10^3 - 10^4$ different speckle realisations. To reduce as much as possible the computation time, all programs are written in C language with a Fast Fourier Transform optimized on the NVIDIA GPU (Govindaraju & Manocha 2007) under the Linux architecture. Under such conditions, 4 hours of computing time are needed to perform 16384 short coronographic images, including turbulence and photometric noise.

5. Nulling performance for a coronagraphic device on an interferometer

It is possible to recombine an interferometer either with a coronagraphic (Riaud et al. 2001b, 2002) or with a nulling system (Lay 2004, 2005). The final performance, in terms of total rejection, will be limited for any kind of recombinations by two strong effects: (a) the stellar leakage (the case studied in the current work) and (b) the chromatism of the π phase-shift. However, the latter limitation only becomes significant to reach huge rejection ratios ($R_c > 10^5$) that are needed for the search of Earth-like planets with space-borne interferometers (Wallner et al. 2006). In the following sections we will study some other nulling-related limitations, that we describe with the general term "instrumental nulling" issues.

5.1. Instrumental nulling

- *Phase-mask transition.* There are still some limitations in the manufacturing of phase-mask coronagraphs, such as the FQPM or the OVVC2/AGPM (Optical Vectorial Vortex Coronagraph of charge 2). Using a FQPM coronagraph, it has been demonstrated that $R_c > 10^5$ (Riaud 2003) can be achieved through a narrow band on a visible workbench.

  On a ground-based telescope facility, $R_c > 4 \times 10^2$ have been achieved with an OVVC2

(Swartzlander et al. 2008; Mawet et al. 2009).

- *Cross-talk between the sub-apertures in the Fizeau mode.* Indeed, the starlight rejected by each sub-aperture contaminate the other ones. This effect is very small: for a ratio $B_{out}/d_{out} > 16$, it does not affect the rejection ratios at the 10^6 level (see Eq. 19).

- *Central obscuration.* Phase-mask coronagraphs, such as AGPM/OVVC2/FQPM, are sensitive to the central obscuration of the telescope. Indeed, for a circular pupil, the rejection is perfect in the theoretical case (Riaud 2003; Mawet et al. 2005). A central obscuration strongly reduces the energy located in the central airy disk of the telescope's diffraction pattern. This reduction directly affects the coronagraph's rejection. Unlike Jenkins (2008) who develops the amplitude of the PSF using a Bessel series, the residual intensity due to the central obscuration a can be easily calculated via the energy conservation law (Riaud 2003). The residual energy, E_{res}, is given directly by the surface ratio between the central obscuration and the entire pupil and the result is:

$$
\begin{aligned}
E_{res}(a, r_d) &= 0 \quad r < a \qquad\qquad (30) \\
E_{res}(a, r_d) &= \pi a^2 (1 - \frac{a^2}{r_d^2}) \quad a < r < r_d \\
E_{res}(a, r_d) &= \pi (1 + \frac{a^4}{r_d^2} - 2a^2) \quad r > r_d
\end{aligned}
$$

where r_d is the diaphragm radius. The diaphragm chosen in our VLT simulation with single-mode filtering possesses an outer diameter of 90%, in pupil units. Indeed, single-mode fiber filtering attenuates the impact of the central obscuration. This configuration allows a maximum total nulling ratio of ≈ 1000 in full H-band because the diaphragm optimization is limited by the coronagraphic diffraction limitation. This limitation is mainly due to the presence of manufacturing defects in the center of the phase-mask and chromaticity issues (Mawet et al. 2009). The impact of the central obscuration is reduced thanks to the use of monomode-fibers. Due to the relatively poor fringe tracker efficiency (all simulations are given for a conservative $\lambda/3$ rms accuracy), the median nulling factor is generally lower than 40 (see Fig. 4).

5.2. Optical throughput limitation

The first limitation is due to the coupling efficiency of single-mode filtering which is 25%. This number is obtained by computing the injection efficiency of a beam having a perfect Strehl ratio into a single mode fiber. This instrumental configuration allows a high instrumental stability and it must be preserved. In terms of optical throughput, the Fizeau recombination combined with the densified mode [2] seems to be more efficient than other systems. Indeed, the Fizeau recombination is a much simpler optical system, that allows a low residual wavefront error. The densified pupil is only applicable before the coronagraph if the sub-apertures are off-axis (i.e. no central obscuration) and a pupil-edge continuity is required after the densification process (i.e. square or hexagon sub-apertures). This is not our case, as we are considering two circular UT-VLT pupils. In the context of UT-VLT coronagraphic nulling, the entrance pupil must not be densified, as it would increase the cross-talk between the two pupils. We can notice that the FQPM coronagraph does not suffer from cross-talk effects in the case where four sub-apertures are mapped on a cross configuration with a pupil separation of $2\sqrt{2}$, in pupil radius units.

The classical Bracewell nuller can be used in the same way, but the beam recombination with cascaded beamsplitters (depending on the number of sub-apertures) requires a lot of photons and provides a low stability due to the huge optical complexity. This configuration is not considered in our study. Two different optical schemes can be chosen to overcome the aforementioned drawbacks: integrated optics and off-axis single mode fiber recombination can be efficient ways to increase the throughput and stability for nulling interferometry in the near infrared. The Palomar Fiber Nuller (Haguenauer & Serabyn 2006; Martin et al. 2008)

---

[2]In our case, the Fizeau recombination is combined with a phase-mask coronagraph and a pupil densification at the last stage, after a starlight filtering by a Lyot stop.

and MAII (Buisset et al. 2006) are examples of instruments with simpler recombination system.

6. Statistical data analysis

In this section we present a statistical analysis using a large number of short-exposure frames to estimate possible biases in the stellar radius measurements. The principle is to compare the rejection statistics measured in different data sets corresponding to a possible variation of the stellar diameter during the Cepheid period. The mathematical approach is that of a classical, "dark speckles" analysis: we calculate the statistical distribution of the rejection factor $R_{c,\alpha}$ in n different coronagraphic images, obtained during photometric acquisition including instrumental and stellar diameter effects. If we define $R_{c,\alpha}$ as beeing the rejection factor in a coronagraphic image, D_1 the photodiode in the pupil plane, and D_2 the high speed detector in the full field of view (see Fig. 1), $R_{c,\alpha}$ is calculated according to the formula:

$$R_{c,\alpha} = \frac{\phi(D_1) + \sum_{pixels} M_B.[\phi(D_2)]}{\sum_{pixels} M_B.[\phi(D_2)]} \qquad (31)$$

where $\phi(D_1)$ and $\phi(D_2)$ are respectively the fluxes measured by the photodiode in the pupil plane and the flux measured on the detector and M_B is the photometric attenuation induced by the coronagraphic mask. To calculate more precisely the rejection ratio, the mask's rejection M_B is assessed using the best frames (see Sect. 6.1) with an appropriate threshold on the photometric data to enhance the image shape.

6.1. Nulling histogram retrieval

During an observation, the null depth fluctuates with time as a function of the different error sources. Therefore, it becomes more diffcult to recover the astrophysical null R_α. The method we propose here is based on the statistical analysis of the probability distribution function (PDF) of the null depth.

6.1.1. Photon-noise limitation

As the majority of the stellar targets are fainter than sixth magnitude in the H-band, it is necessary to stack short exposures to generate an improved signal-to-noise image. Indeed, if instead,
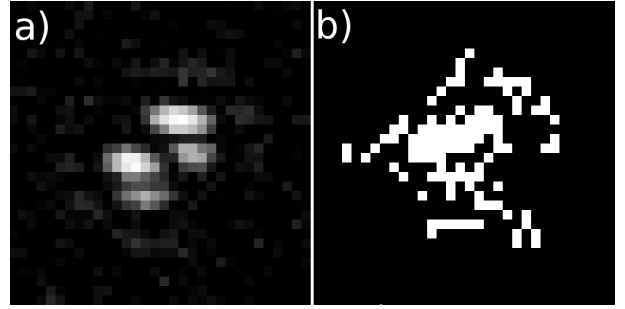

Fig. 3.— *Left panel*: *H*-band image of the Cepheid EN TrA, generated by stacking some 100 individual frames (5ms exposure time per frame). *Right panel*: binary mask M_B of the best image used to derive the nulling factor on the central part of all coronagraphic images.

we increase the exposure time for the individual coronagraphic images, we average the fast fluctuations of the instrumental rejection ratio and reduce the probability to reach very high rejections. Signal to noise ratio considerations indicate that the limiting magnitude for the proposed technique is about 7.5 in full H-band.

6.1.2. Coronagraphic data analysis

Let us explain the nulling histogram retrieval procedure for a proper stellar diameter estimation. In the case of a pulsating star observed with an interferometric coronagraphic system, the stellar diameter varies between two measurements. If $R_{\tau 1}$ and $R_{\tau 2}$ are two sequences of rejection ratio measurements at different epochs, a simple ratio of their distributions is sufficient to identify the one that contains the smaller number of frames with high rejection ratios ($R_c > 40$ in our case where the fringe tracker have $\lambda/3$ rms accuracy) for the biggest stellar diameter. Having carefully removed the appropriate bias level (background level), the data is reduced as follows:

(a) the rejection ratio of each coronagraphic image with $M_B = 1$ over the whole detector image is first calculated

(b) the best frame in terms of rejecion ratio is taken, in order to create the new binary mask M_B (see Fig. 3).

(c) the rejection ratio is computed on the remaining images using the new binary mask M_B obtained in the first analysis.

In order to enhance the stellar diameter measurement, it is necessary to limit our analysis to rejection ratios R_c greater than the median value (see Fig. 4) as this part of data is more affected by the stellar diameter effect.

Before illustrating our data analysis on a real Cepheid star (EN TrA, see Sect. 7.1), we must determine the mathematical form of the histogram function. This theoretical step is mandatory in order to obtain an accurate unbiased diameter measurement.
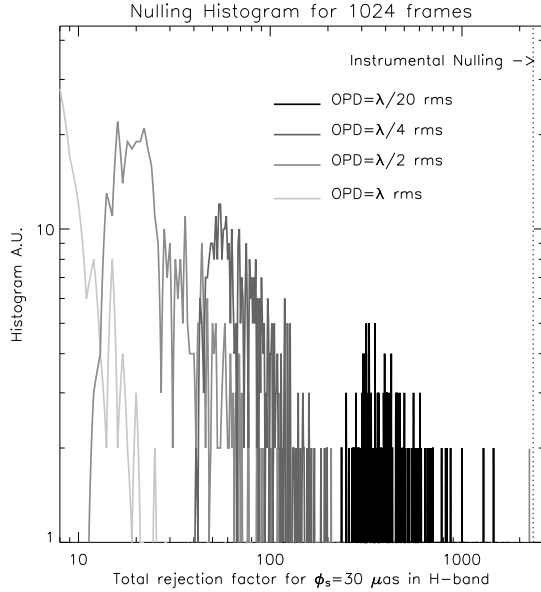

Fig. 4.— Nulling histogram of 1024 different interferometric coronagraphic frames as a function of the total rejection factor, for four cases of OPD errors between the two apertures. In the simulations a stellar diameter of $30\mu as$ in the H-band ($0.011\lambda/B$) has been considered. The significantly improved behavior in the stabilization regime when using a fringe tracker is clearly visible ($OPD < \lambda/2$ rms)
.

6.1.3. Rejection function

The rejection function is defined as the ratio $R_c = I_+(t)/I_-(t)$ where $I_+(t)$ and $I_-(t)$ are respectively the overall incoming intensity of the light feeding the instrument and the nulled output intensity after introduction of the coronagraph. It can be expressed as a function of the different fluc-

tuating sources of noise that influence its value. From this general form of the rejection function, depending on the intensity mismatch $di(t)$, the phase error $\Delta\phi(t)$ and the relative polarizarion rotation angle ϱ of the interferometric beams, it is straightforward to derive the instrumental rejection function. This analysis in terms of null depth function, $(1/R_c)$ has been developed in the general case of a nulling interometer by Hanot et al. (2010).

Indeed, if $\Delta\phi(t)$, $di(t)$, ϱ are small, in the case of a two aperture interferometer, the rejection function is

$$R_c = \frac{I(t)}{(\Delta\phi(t)^2/4 + di(t)^2/16 + \varrho^2/4)} \quad (32)$$

From Eq. 32, the rejection taking into account the astrophysical contribution is then simply given by

$$R_{c,\alpha} = R_c + I(t)R_\alpha \quad (33)$$

Among the three fluctuating terms in equation 32, the phase error is a combination of both the fringe tracker residuals and turbulence fluctuations. Indeed, fringe trackers (FT) are not able to correct for the fastest phase perturbations induced by the atmosphere. As a result, the phase error $\Delta\phi(t)$ is only corrected for frequencies within the FT range. From a probability distribution point of view, it creates two different distributions in the noise analysis: $\Delta\phi(t) = \Delta\phi_{atm}(t) - \Delta\phi_{ft}(t)$.[3]

For the sake of simplicity, we will also consider from now on that the polarization effect is static and small compared to the other terms and therefore does not contribute to the statistical distribution ($\varrho = 0$).

6.1.4. Probability distribution function

To analyse the probability distribution function (PDF) of the coronagraphic rejection factor, we must take into account the main statistical errors during observations. We consider in this analysis that $\Delta\phi(t)$, $di(t)$, $I(t)$ follow normal distributions, with means μ_i and standard deviations σ_i. To calculate the final probability distribution function

---

[3]If $\Delta\phi_{atm}(t)$ and $\Delta\phi_{ft}(t)$ are independent normal variables following the law $\aleph(\mu_{atm}, \sigma_{atm}^2)$ and $\aleph(\mu_{ft}, \sigma_{ft}^2)$, then $\Delta\phi(t) = \Delta\phi_{atm}(t) - \Delta\phi_{ft}(t)$ is also a normal distribution and follows the law $\aleph(\mu_{atm} + \mu_{ft}, \sigma_{atm}^2 + \sigma_{ft}^2)$

of equation 33, we make use of two theorems:

(1) If two random variables A and B are independent with probability density functions equal to f_a and f_b respectively (Rohatgi 1976; Pelat 1996):

$$f_{a/b}(C) = \int_{-\infty}^{+\infty} |B| f_a(B.C).f_b(B)dB \qquad (34)$$

where the variable substitution $C = A/B$ has been applied.

(2) If A and B are two independent random variables with densities f_a and f_b respectively (Rohatgi 1976; Pelat 1996):

$$f_{a+b}(C) = \int_{-\infty}^{+\infty} f_a(A).f_b(C-A)dA \qquad (35)$$

where we have used the following variable substitution: $C = A + B$. Therefore, the density function of a sum of two independent random variables is simply the convolution of the densities of these two variables.

Using these two principles, we can find an analytical solution to the instrumental rejection factor, $R_c = I/(di^2/16 + \Delta\phi^2/4)$ (neglecting the polarization term).

First of all, we know that $I(t)$, $di(t)$ and $\Delta\phi(t)$ are gaussian distributions, therefore, we have:

$$f_i(z) = \frac{e^{\frac{-(z-\mu_i)^2}{2\sigma_i^2}}}{\sqrt{2\pi}\sigma_i} \qquad (36)$$

where i corresponds respectively to I, di and $\Delta\phi$ for the three distributions. The expression for both di^2 and $\Delta\phi^2$ densities is given by (Pelat 1996) in the case of pure gaussian distributions:

$$f_i\left(\frac{z^2}{\xi_i}\right) = \frac{e^{-(\xi_i z + \mu_i^2)/2\sigma_i^2}}{\sqrt{2\pi}\sigma_i\sqrt{\xi_i z}} . \cosh\left(\frac{\mu_i\sqrt{\xi_i z}}{\sigma_i^2}\right) \qquad (37)$$

where the ξ_i are the coefficients multiplying $\Delta\phi^2$ and di^2 in equation 33 ($\xi_{\Delta\phi} = 4, \xi_{di} = 16$). Now that we have the different expressions for the three random variables I, di^2 and $\Delta\phi^2$, we can first find the expression of $(di^2/16 + \Delta\phi^2/4)$ by

substituting (37) into (35).

$$f_{di^2+\Delta\phi^2}(y) = \frac{e^{-\left(\frac{\mu_{\Delta\phi}^2}{\sigma_{\Delta\phi}^2} + \frac{\mu_{di}^2}{\sigma_{di}^2}\right)}}{4\pi\sigma_{\Delta\phi}\sigma_{di}} e^{-\left(\frac{y}{2\sigma_{di}^2}\right)}$$
$$\times \int_0^{2\pi} \frac{x^{-1/2}e^{-\frac{x}{2}\left(\frac{1}{\sigma_{\Delta\phi}^2}+\frac{1}{\sigma_{di}^2}\right)}}{\sqrt{y-x}}$$
$$\times \cosh\left(\frac{\mu_{\Delta\phi}}{\sigma_{\Delta\phi}^2}\sqrt{x}\right)\cosh\left(\frac{\mu_{di}}{\sigma_{di}^2}\sqrt{y-x}\right)dx \qquad (38)$$

the instrumental rejection ratio R_c is then obtained by using the fundamental statistic relations (34) and (38):

$$\begin{aligned}
f_{R_c}(z) &= \frac{e^{-\left(\frac{\mu_{\Delta\phi}^2}{\sigma_{\Delta\phi}^2}+\frac{\mu_{di}^2}{\sigma_{di}^2}\right)}}{\sqrt{2}\pi^{\frac{3}{2}}\sigma_{\Delta\phi}\sigma_{di}\sigma_I} \int_0^{+\infty}\int_0^{2\pi} \frac{x^{-1/2}e^{-\frac{x}{2}\left(\frac{1}{\sigma_{\Delta\phi}^2}+\frac{1}{\sigma_{di}^2}\right)}}{\sqrt{y-x}} \\
&\times \cosh\left(\frac{\mu_{\Delta\phi}}{\sigma_{\Delta\phi}^2}\sqrt{x}\right)\cosh\left(\frac{\mu_{di}}{\sigma_{di}^2}\sqrt{y-x}\right)dx \\
&\times y\,e^{-\left(\frac{y}{2\sigma_{di}^2}\right)}e^{-\left(\frac{(zy-\mu_I)^2}{2\sigma_I^2}\right)}dy
\end{aligned} \qquad (39)$$

where x and y are respectively the continuous random variables of $f_{\Delta\phi}(x^2)$ and $f_{di}(y^2)$ while z is the result of the variable substitution $z = y\,w$, where w is the variable of $f_I(w)$. Finally, adding the astrophysical rejection ratio to the instrumental one mathematically corresponds to convolve the R_c density with a Dirac distribution $\delta(R_\alpha)$ (see Eq. 4), with R_α being the astrophysical rejection limitation. Therefore, the final rejection ratio probability distribution taking into account both the instrumental and astrophysical limitations, $f_{R_{c,\alpha}}(z)$, is:

$$f_{R_{c,\alpha}}(z) = f_{R_c}(z') \qquad z' = \frac{zR_\alpha}{z+R_\alpha} \qquad (40)$$

If we replace R_α into Eq. 4, the new position z' of the full statistic with respect the purely instrumental nulling $f_{R_c}(z)$ becomes:

$$2\alpha(\lambda/B) = \frac{4\sqrt{3}}{\pi}\sqrt{\frac{z-z'}{zz'}} \qquad (41)$$

The equation 40 is very important to recover the astrophysical rejection ratio R_α in the entire statistic distribution $f_{R_{c,\alpha}}$. Indeed, once the R_α

14

corresponding to the best fit of the rejection distribution $f_{R_c,\alpha}$ is found, it is straightforward to derive the stellar angular diameter using Eq.4. The fitting procedure presented hereafter uses the statistical distribution to recover the angular stellar diameter with a sub-resolution precision.

6.1.5. Fitting procedure of the statistical distribution

An increase of the stellar diameter will shift the rejection factor histogram towards lower values and will reduce dramatically the number of frames with rejection factor larger than $R_c \approx 40$ depending on the fringe traker accuracy (see Fig. 5). The variation of the peak position of the nulling PDF is highly correlated with the stellar diameter if the intensity fluctuation is less than 10%, due to the photometric monitoring in the pupil plane.
The PDF fitting is performed using the non linear Levenberg-Marquardt method. We use a modified "mpfit" procedure provided by (Markwardt 2008; Moré 1977) with the GSL library (Galassi et al. 2009; Piessens et al. 1983) that provides the numerical integration needed to fit the final nulling PDF. In order to accelerate the convergence of the Levenberg-Marquardt algorithm we must restrict the different fitting parameters to the most probable ranges of values. For the means and standard deviations of the intensity mismatch and phase errors, we have defined the following ranges:

$$0 < \mu_{\Delta\phi} < 0.5 \quad 0 < \mu_{di} < 15\% \quad \sigma_{\Delta\phi} > 0 \quad \sigma_{di} > 0$$

6.2. Presence of a faint companion or a circumstellar disk

Coronagraphic techniques are generally used to enhance the sensitivity to faint companions or circumstellar structures around a star. We study here the effect of the presence of a faint companion or a circumstellar disk around the target on the determination of its angular diameter. Indeed, this detection can contaminate our data and, consequently, the analysis of the stellar leakage to retrieve the radius of the target. The observed field of view corresponds to the diameter of the Airy pattern of the sub-aperture ($\approx 50\,mas$ in the H-band for a 8 meter class telescope) and the whole information is "compressed" in the densified field of view (3 fringes) due to the poor (u,v) coverage obtained by only two apertures. It is possible to increase the number of resolution elements used to reconstruct the source by rotating the interferometer's baseline during the observations. For that, we consider that either the companion or the circumstellar disks signals are under the detection limit (3σ) of the instrument. Indeed, if either a companion or a disk is clearly visible (signal $> 3\sigma$), two different situation are possible:
(1) if it is a companion or any point-like off-axis source, it is possible to properly modify the mask M_B to remove the off-axis contribution and achieve an improved rejection analysis.
(2) in the case of extended features, it is not possible to modify the mask. However, if these faint features are below the direct detection confidence, it becomes easier to prove that the faint features around the star are constant in terms of photometric result, and appear as an offset in the data. This photometric "excess" is generally constant with respect to the photon noise and a proper bias calibration of the flux becomes the key to retrieve the stellar diameter information. In this case, the system possesses two free parameters (the stellar radius, and the photometric "excess").

7. Application: Cepheid pulsations measurement at the VLTI

The problem to measure stellar pulsations of Cepheids is twofold: (i) they are only marginally resolved using the existing baselines and (ii) the pulsation of their amplitudes are rather weak ($\approx 10 - 15\%$). However, using the Palomar Testbed Interferometer it has been possible to detected the pulsation of ζ Gem (Lane et al. 2000), one of the most distant galactic Cepheid ever discovered. Still, the level of significance remains weak and more observations are needed to improve these first results. Our technique can increase this significance of the detection for relatively close Cepheids variables that have been already observed (e.g. δ Cep, ζ Gem (Kervella et al. 2001), η Aql (Lane et al. 2002)) but can also allow us to observe more distant targets (see Table 1).

Using our method, there are several factors that can increase the significance of diameter variation in Cepheids.One of the most critical one is the accuracy to which the photometric calibration and reduction is performed. For example, the spectral response of the photodiode has to be carefully

calibrated, to minimize observational skew. Additionally, Cepheid observations can be optimized by choosing an unresolved reference star, close to our principal target, that shall act as a nulling calibrator. Finally, it is still feasible to observe stars with known diameter information, obtained with "classical" interferometric visibility measurements (see Sect. 8.1). These observations can serve to set an absolute stellar calibrator for our statistical method used on the coronagraphic images.

Table 1: Example of distant galactic Cepheids (Berdnikov et al. 2000)

Name	EN TrA	VZ Pup	AD Pup	AQ Pup
Stellar type	F2Ib	F7.5	F8	F5Ib
Distance in kpc	7.04	4.62	4.09	2.89
Diameter in μas	75	142	170	200
I_c mag	7.8	8.3	8.7	7.1
J mag	7.1	7.1	7.7	5.9
H mag	6.6	6.6	7.2	5.3
K mag	5.9	6.5	7.1	5.1

7.1. Simulations results with the EN TrA star

We have performed a nulling mode simulation for the most distant Cepheid of our sample: EN TrA (see Tab. 1). Throughout our study we considered a uniform diameter varying from 68 to 78 μas (see Table 2) and a VLTI-UT configuration using a 130 m baseline. The star has an H-band magnitude of 6.6. Without coronagraphic attenuation, it corresponds to an incoming total signal of 15 800 photons for 0.5 s of exposure time and a spectral resolution of 10 (the total overall transmission is 3%). Its properties, together with those of some better candidates for using our method, are presented in Table 1.

Because the number of photons arriving to the detector per exposure time is low, it is necessary to stack a large number of frames (typically 100 for this example) in order to increase the SNR. The quality of our data depends on the number of measurements having high rejection factor. To increase this number, it is necessary to stabilize the fringes that move rapidly because of the atmospheric turbulence. On the UT's, the fringe stabi-

Table 2: Limitation of the rejection factor R_α due to the finite extent of the stellar diameters. This limitation is computed in H-band for different values of the stellar angular diameter (α).

Diameter in μas	68	72	75	78
Diameter (α) in λ/B	0.0259	0.0275	0.0286	0.0298
R_α (Eq 3)	1810	1600	1480	1370

Table 3: Table summarizing some key numbers and properties of the interferometer such as: (i) the different filter's wavebands (ii) the central wavelength corresponding to theses filters (iii) the angular separation between two interferometric fringes (iv) the speckle lifetime τ in ms (v) the detector frequencies in the different bands and (vi) the readout noise of these detectors in electrons.

Filter	I	J	H	K
Wavelength μm	0.8	1.2	1.65	2.2
λ/B in mas	1.26	1.9	2.6	3.5
τ in ms	3	6	12	20
Detector Frequency in kHz	1	0.4	0.2	0.1
Readout noise (e-)	5	6	6	6

lization depends on both the low order corrections of the individual telescopes adaptive optics (Strehl ratio lower than 30% at 1.65 μm) and of the VLTI fringe tracker ($\lambda/3$ rms at 1.65 μm). When used with the AT's, this AO system is replaced by simpler tip/tilt mirrors (STRAP). In both cases such systems improves the detectability due to the partial correction of the tip-tilt errors in each sub-aperture. Indeed, it decreases the number of bad frames due to poor centering (see Fig. 4). The frequency of the photodiodes and the NICMOS detector is 200 Hz and must be compared to the supposed speckles lifetime which is $\sim$12 ms in H-band (see Table 3). For each observational simulation we generate 4096 individual average exposures (2048 s of total exposure time per fixed stellar diameter). Five diameter measurements, obtained during the pulsating period of the Cepheid, resulted on five values spanning from 68 to 78 μas depending on the pulsation phase. The influence of the atmospheric conditions has been taken into

account by modifying the amplitude of the turbulence between each dataset (we assume a Taylor turbulence, with a layer displacement having a speed of 8 m/s). The detector's response has also been modified during the five data sets. The influence of the stellar diameter on the global statistics of the coronagraphic nulling is clearly visible in Fig. 5. **Although the size of the star's diameter does not seem to play an important role on the histogram shape for low rejection factors, its importance becomes more prominent for the measurement at larger rejections factors.**

Fig. 5.— Nulling histogram for 4096 different interferometric coronagraphic nulling H-band images on the Cepheid EN TrA star. During the simulations, five stellar diameters with values between 68 to 78 μas were measured. The figure shows the histogram of the total rejection factor as a function of the stellar diameter. In this figure only the data with a nulling ratio greater than the median of the histogram are shown (50% of initial frame number).

7.1.1. Fitting the nulling histograms

Such a fitting example is presented in Fig 6 for a value of the EN TrA stellar diameter of 68 μas. During our statistical analysis of the rejection factor histogram, we fit the full statistic with the

phase and the intensity mismatch error distributions ($\Delta\phi, di$). The phase and intensity mismatch distributions corresponding to the least square of the fitting procedure for the four different stellar diameters (see Fig.5) are :
0.385 ± 0.072 wave rms for ($\mu_{\Delta\phi}, \sigma_{\Delta\phi}$) and $8.3\% \pm 5.4\%$ rms for the amplitude mismatch error (μ_{di}, σ_{di}). The intensity fluctuation $I(t)$ during the stellar diameter retrieval is monitored directly by the the photodiodes system ($\sigma_I = 2\%$ rms) and is therefore considered as known during the fitting process. The values of the phase errors retrieved by the histogram fitting method (see Table 4) seems to be efficient as they are very close to the input parameters of the Monté-Carlo numerical simulation.

Table 4: Retrieved fitting parameters

Stel. Diam. (μas)	68	72	75	78
$\mu_{\Delta\phi}$ in wave	0.308	0.365	0.41	0.46
$\sigma_{\Delta\phi}$ in wave rms	0.076	0.064	0.071	0.08
μ_{di} in %	8	9	10	6.5
σ_{di} in % rms	2	3	10	6.5
σ_I in % rms	2	2	2	2
Retreived Diam. (μas)	68.4	71.6	75	78

Once the astrophysical rejection corresponding to the optimal fit of the dataset distribution is found, they are converted into stellar angular diameters using Eq. 4. Table 4 shows a summary of the stellar diameter which are measured compared to the one simulated in the model. For all cases, the error on the measured diameter is small as they are always $< 0.6\,\mu$as. The rms error on the angular diameter for the 4 simulations is $0.41\,\mu$as which corresponds, in tems of λ/B to accuracies lower than $\lambda/1000B$.
Note that for on-sky measurements, the observation of a calibrator star of well known diameter (of $\sim 300\mu$as) can increase the accuracy of the method. Indeed, by doing so, it is possible to get rid of eventual systematic bias that are not corrected by the statistical reduction method.
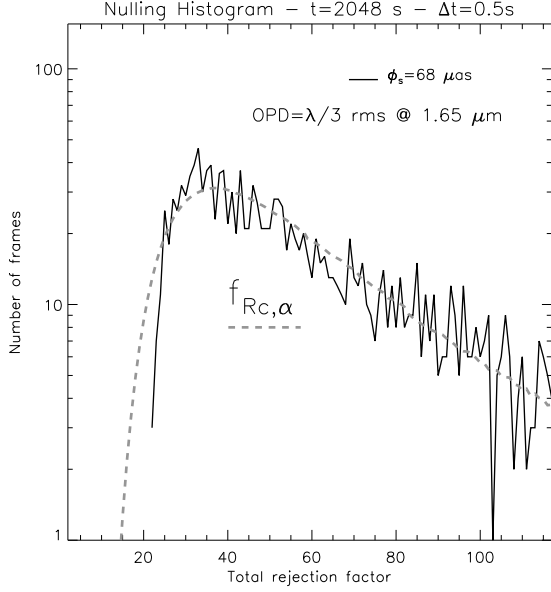
Fig. 6.— Nulling histogram of 4096 different interferometric coronagraphic nulling H-band images for a stellar diameter of 68 μas. The figure shows the histogram of the total rejection factor for data with a rejection factor greater than the median value. The dashed line trace the fitting function $f_{R_c,\alpha}$ that characterize the global nulling statistic.

7.2.   Simulations with a circumstellar companion or disk

In this section we perform the simulation for the same Cepheid in presence of a faint companion or a disk around it. We test the stellar diameter retrieval quality with respect to the magnitude difference, Δm, between the star and the faint companion/disk, where $5 \leq \Delta m \leq 9$. A $\Delta m = 5$ corresponds to the detection limit of the disk or companion at the 3σ level with our technique. The accuracy of the proposed method remains good, with an error of $6\,\mu as$ PTV for the brightness companion/disk and less than $1\,\mu as$ PTV for the fainter case. The simulation results are presented in Figs. 7, 8.

8.   Discussion

This paper demonstrates the possibility to improve the accuracy of stellar diameter measurements with a coronagraphic device by mean of
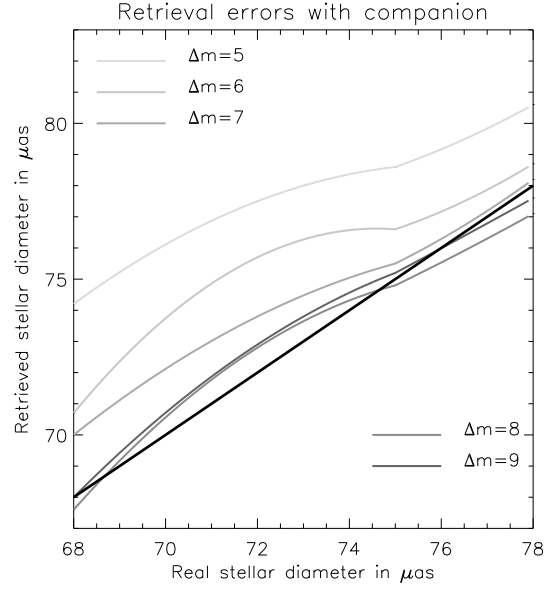

Fig. 7.— Retrieval errors obtained on the 4096 different interferometric coronagraphic nulling H-band images for the Cepheid variable EN TrA star with a low mass star as a companion. The magnitude difference between the primary star and the companion ranges between 5 and 9. $\Delta m = 5$ correspond to the instrument detection limit at the 3σ level. The figure shows the five retrieved angular stellar diameters as a function of the real value, for different luminosity ratios. The black line corresponds to the exact solutions.

statistical data analysis. However, despite the advantages proposed with this configuration, interferometry in general still suffers from two limitations:

(a) The detection noise is significant due to the very short exposure times.

(b) The fringe tracking accuracy is rather low (typically $\sim \lambda/3$ rms).

The example presented in section 7 was based on a simulation of 4096 exposures, with 68 minutes of total integration time (equally distributed between the target and reference star). The results presented in the previous paragraph can be further improved by observing a calibrator star of well known diameter. Doing so, it is possible to get rid of eventual instrumental bias that are not taken into account by the statistical data reduction (e.g. the rotation of polarization). It is worth
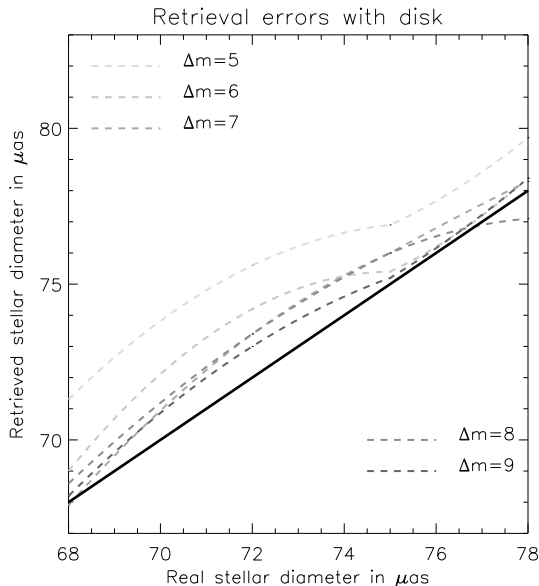
Retrieval errors with disk

Fig. 8.— Retrieval errors obtained for the Cepheid variable EN TrA star with a circumstellar disk (face-on). The difference of magnitude of the disk is 5 to 9 for the flux total. The figure shows the five retrieved angular stellar diameters with respect to its actual value for different luminosity ratios.

mentioning that only reference stars with a diameter in the range $200 - 400\,\mu as$ are usable in the coronagraphic mode. Indeed, large stellar diameters strongly limit the rejection factor ($R_c < 5$) of the coronagraphic mode. In this case, classical visibility measurement can be more efficient than the nulling mode.

8.1. Classical visibility vs Coronagraphic retrieval

We can compare the gain of our technique with the sub-resolution visibility fitting procedure used in classical interferometry (Lachaume 2003).Indeed, a classical long-baseline interferometer, such as CHARA (Baines et al. 2008), uses a fitting procedure to retrieve the Uniform and Limb-darkened stellar diameter (UD,LD). The data obtained with this interferometer for the case of a 330 m baseline in H and K-bands on 46 stars (reference and science) lead to the following results (in λ/B unit): Uniform angular diameter have been measured down to $\lambda/6B$. The error on these measurement is

on average of $\lambda/43B$ and goes down to $\lambda/172B$ in the best case. The gain with a coronagraphic system remains important for small stellar diameters (typically $\sim \lambda/40B$). Indeed, for EN TrA star, we have been able with our method the measure an angular diameter of $\sim \lambda/35B$ with a precision of $\lambda/1310B$. With the VLTI and the UTs, the limiting magnitude of $I = 9$ opens wide possibilities to study distant Cepheids (2 to 7 Kpc) in the Milky-Way.

8.2. Nulling interferometry

The technique proposed in this work is also applicable to the case of nulling interferometer experiments such as GENIE on the VLTI (Gondoin et al. 2003) or the fiber nuller (Haguenauer & Serabyn 2006; Martin et al. 2008). The main difference with the configuration proposed in the current paper is that the FoV of Genie is limited by one resolution element (while in our configuration it is 3 resels). Some studies by Hanot (Hanot et al. 2010, in prep) on the fiber nuller points to a better stellar diameter calibration using this technique than with classical methods.

9. Conclusions

The present article introduces a new approach to tackle the problem of measuring stellar diameters, using a coronagraphic interferometer. Such a configuration is far more accurate (by a factor of 100 in the speckle mode) compared to the "classical" visibility measurements, and potentially even more accurate if a fringe tracker is used. Direct measurements of angular diameter variations of Cepheids avoids the problem of color versus surface brightness calibration in the distance determination (Fouqué et al. 2007; Marengo et al. 2003). The suggested configuration is also applicable to previous Cepheids measurements, to obtain more precise measurements of their pulsations. Additionally, our technique can also be implemented for more distant Cepheids ($\sim 2 - 7$ kpc) Interferometric measurements of more distante Cepheids diameter can improve our knowledge on the Period-Luminosity relation, which has a direct impact on the extragalactic distance scale measurements.

(Ghent University), J. Surdej , Jean-Pierre Swings and O. Absil (IAGL) for the manuscript corrections.

REFERENCES

Armstrong, J. T., Nordgren, T. E., Germain, M. E., Hajian, A. R., Hindsley, R. B., Hummel, C. A., Mozurkewich, D., & Thessin, R. N. 2001, AJ, 121, 476

Baines, E. K., McAlister, H. A., ten Brummelaar, T. A., Turner, N. H., Sturmann, J., Sturmann, L., Goldfinger, P. J., & Ridgway, S. T. 2008, ApJ, 680, 728

Berdnikov, L. N., Dambis, A. K., & Vozyakova, O. V. 2000, A&AS, 143, 211

Bonaccini, D., Gallieni, D., Biasi, R., Gori, F., Ghioni, M., Trottier, C., & Hubin, N. 1997, in Presented at the Society of Photo-Optical Instrumentation Engineers (SPIE) Conference, Vol. 3126, Society of Photo-Optical Instrumentation Engineers (SPIE) Conference Series, ed. R. K. Tyson & R. Q. Fugate, 580–588

Buisset, C., Rejeaunier, X., Rabbia, Y., Ruilier, C., Barillot, M., & Karlsson, A. 2006, in IAU Colloq. 200: Direct Imaging of Exoplanets: Science & Techniques, ed. C. Aime & F. Vakili, 309–312

Coudé Du Foresto, V. 1997, Academie des Science Paris Comptes Rendus Serie B Sciences Physiques, 325, 177

Delage, L., & Reynaud, F. 2001, Opt. Express, 9, 267

Feast, M. W., Laney, C. D., Kinman, T. D., van Leeuwen, F., & Whitelock, P. A. 2008, MNRAS, 386, 2115

Ferrarese, L., Mould, J. R., Stetson, P. B., Tonry, J. L., Blakeslee, J. P., & Ajhar, E. A. 2007, ApJ, 654, 186

Fizeau, H. 1868, CR. Acad. Sci. Paris,t, 68, 932

Fouqué, P., Arriagada, P., Storm, J., Barnes, T. G., Nardetto, N., Mérand, A., Kervella, P., Gieren, W., Bersier, D., Benedict, G. F., & McArthur, B. E. 2007, A&A, 476, 73

Galassi, M., Davies, J., Theiler, J., Gough, B., Jungman, G., Alken, P., Booth, M., & Rossi, F. 2009, GNU Scientific Library Reference Manual (3rd Ed.) (Network Theory Ltd), 73

Gondoin, P., Absil, O., Fridlund, C. V. M., Erd, C., den Hartog, R. H., Rando, N., Glindemann, A., Koehler, B., Wilhelm, R., Karlsson, A., Labadie, L., Mann, I., Peacock, A. J., Richichi, A., Sodnik, Z., Tarenghi, M., & Volonte, S. 2003, in Presented at the Society of Photo-Optical Instrumentation Engineers (SPIE) Conference, Vol. 4838, Interferometry for Optical Astronomy II. Edited by Wesley A. Traub . Proceedings of the SPIE, Volume 4838, pp. 700-711 (2003)., ed. W. A. Traub, 700–711

Govindaraju, N. K., & Manocha, D. 2007, Parallel Comput., 33, 663

Haguenauer, P., & Serabyn, E. 2006, Appl. Opt., 45, 2749

Hanot, C., Mennesson, B., Serabyn, E., Martin, S. R., Liewer, K., Loya, F., Mawet, D., Riaud, P., & Absil, O. 2010, In prep.

Hicks, C., Kalatsky, M., Metzler, R. A., & Goushcha, A. O. 2003, Appl. Opt., 42, 4415

Jenkins, C. 2008, MNRAS, 384, 515

Kervella, P., Coudé du Foresto, V., Perrin, G., Schöller, M., Traub, W. A., & Lacasse, M. G. 2001, A&A, 367, 876

Labeyrie, A. 1970, A&A, 6, 85

—. 1995, A&A, 298, 544

—. 1996, A&AS, 118, 517

Lachaume, R. 2003, Astronomy and Astrophysics, 400, 795

Lane, B. F., Creech-Eakman, M. J., & Nordgren, T. E. 2002, ApJ, 573, 330

Lane, B. F., Kuchner, M. J., Boden, A. F., Creech-Eakman, M., & Kulkarni, S. R. 2000, Nature, 407, 485

Lay, O. P. 2004, Appl. Opt., 43, 6100

—. 2005, Appl. Opt., 44, 5859

Le Bouquin, J.-B., Abuter, R., Bauvir, B., Bonnet, H., Haguenauer, P., di Lieto, N., Menardi, S., Morel, S., Rantakyrö, F., Schoeller, M., Wallander, A., & Wehner, S. 2008, in Presented at the Society of Photo-Optical Instrumentation Engineers (SPIE) Conference, Vol. 7013, Society of Photo-Optical Instrumentation Engineers (SPIE) Conference Series

Le Bouquin, J.-B., Abuter, R., Haguenauer, P., Bauvir, B., Popovic, D., & Pozna, E. 2009, A&A, 493, 747

Macri, L. M., Stanek, K. Z., Bersier, D., Greenhill, L. J., & Reid, M. J. 2006, ApJ, 652, 1133

Marengo, M., Karovska, M., Sasselov, D. D., Papaliolios, C., Armstrong, J. T., & Nordgren, T. E. 2003, ApJ, 589, 968

Markwardt, C. B. 2008, in Astronomical Data Analysis Software and Systems XVIII, ed. D. Bohlender, D. Dowler, & D. A. S. o. t. P. S. F. Durand, Astronomical Data Analysis Software and Systems XVIII, Quebec, Canada, ASP Conference Series

Martin, S., Serabyn, E., Liewer, K., Loya, F., Mennesson, B., Hanot, C., & Mawet, D. 2008, in Society of Photo-Optical Instrumentation Engineers (SPIE) Conference Series, Vol. 7013, Society of Photo-Optical Instrumentation Engineers (SPIE) Conference Series

Mawet, D., Riaud, P., Absil, O., & Surdej, J. 2005, ApJ, 633, 1191

Mawet, D., Serabyn, E., Liewer, K., Hanot, C., McEldowney, S., Shemo, D., & O'Brien, N. 2009, Opt. Express, 17, 1902

Mérand, A., Aufdenberg, J. P., Kervella, P., Foresto, V. C. d., ten Brummelaar, T. A., McAlister, H. A., Sturmann, L., Sturmann, J., & Turner, N. H. 2007, ApJ, 664, 1093

Michelson, A. 1891, Nature, 45, 160

Michelson, A., & Pease, F. 1921, Apj, 53, 249

Moré, J. 1977, The Levenberg-Marquardt Algorithm: Implementation and Theory, Vol. 630 (ed. G. A. Watson (Springer-Verlag: Berlin)), 105

Mourard, D., Bonneau, D., Koechlin, L., Labeyrie, A., Morand, F., Stee, P., Tallon-Bosc, I., & Vakili, F. 1997, A&A, 317, 789

Mourard, D., Tallon-Bosc, I., Rigal, F., Vakili, F., Bonneau, D., Morand, F., & Stee, P. 1994, A&A, 288, 675

Myers, R. A., Farrell, R., Karger, A. M., Carey, J. E., & Mazur, E. 2006, Appl. Opt., 45, 8825

Pelat, D. 1996, Bruits et Signaux (Ecole Docorale de Paris), 351

Piessens, R., deDoncker Kapenga, E., Uberhuber, C., & D., K. 1983, Quadpack: a Subroutine Package for Automatic Integration (Springer Verlag, New York)

Riaud, P. 2003, PhD thesis, Université Paris VI

Riaud, P., Boccaletti, A., Baudrand, J., & Rouan, D. 2003, PASP, 115, 712

Riaud, P., Boccaletti, A., Gillet, S., Schneider, J., Labeyrie, A., Arnold, L., Baudrand, J., Lardiè, O., Dejonghe, J., & Borkowski, V. 2002, A&A, 396, 345

Riaud, P., Boccaletti, A., Rouan, D., Lemarquis, F., & Labeyrie, A. 2001a, PASP, 113, 1145

Riaud, P., Gillet, S., Labeyrie, A., Boccaletti, A., Schneider, J., Rouan, D., Baudrand, J., Arnold, L., Borkowski, V., & Lardière, O. 2001b, in Liege International Astrophysical Colloquia, Vol. 36, Liege International Astrophysical Colloquia, ed. J. Surdej, J. P. Swings, D. Caro, & A. Detal, 85–95

Rohatgi, V. 1976, An Introduction to Probability Theory Mathematical Statistics (Wiley, New York), 141

Rouan, D., Riaud, P., Boccaletti, A., Clénet, Y., & Labeyrie, A. 2000, PASP, 112, 1479

Shaklan, S. 1990, Optical Engineering, 29, 684

Swartzlander, Jr., G. A., Ford, E. L., Abdul-Malik, R. S., Close, L. M., Peters, M. A., Palacios, D. M., & Wilson, D. W. 2008, Optics Express, 16, 10200

Tinetti, G. 2006, Origins of Life and Evolution of the Biosphere, 36, 541

van Belle, G. 2009, in American Astronomical Society Meeting Abstracts, Vol. 214, American Astronomical Society Meeting Abstracts, 411.01−+

van Leeuwen, F., Feast, M. W., Whitelock, P. A., & Laney, C. D. 2007, MNRAS, 379, 723

Vilardell, F., Jordi, C., & Ribas, I. 2007, A&A, 473, 847

Wallner, O., Ergenzinger, K., Flatscher, R., & Johann, U. 2006, in Presented at the Society of Photo-Optical Instrumentation Engineers (SPIE) Conference, Vol. 6268, Advances in Stellar Interferometry. Edited by Monnier, John D.; Schöller, Markus; Danchi, William C.. Proceedings of the SPIE, Volume 6268, pp. 626827 (2006).

Wallner, O., Winzer, P. J., & Leeb, W. R. 2002, Appl. Opt., 41, 637

Wu, G., Jian, Y., Wu, E., & Zeng, H. 2009, Opt. Express, 17, 18782